Article

3D bulk-resolved *g*-wave altermagnetic order parameter in CrSb

https://doi.org/10.1038/s41586-026-10902-z

Received: 15 January 2026

Accepted: 10 July 2026

Published online: 26 August 2026

Open access

Check for updates

Mengmeng Long[1,4], Theodore I. Weinberger[1,4]✉, Zheyu Wu[1,4], Mads F. Hansen[1], Ran Tao[1], Mridul Shrestha[1], Dave Graf[2], Yurii Skourski[3], F. Malte Grosche[1] & Alexander G. Eaton[1]✉

Electronic phases of matter, such as magnetism and superconductivity, are defined and distinguished by their order parameters quantifying the spontaneous symmetry breaking underlying each phase. Simple cases include the uniform magnetization of ferromagnets[1,2] and the isotropic gap function of conventional superconductors[3]. Unconventional superconductors[4] often have a nodal gap function, in which the gap changes sign at nodes on the Fermi surface. This concept of unconventional or nodal order parameter symmetry has recently been extended to numerous magnetic systems[5–8], including altermagnets[9–13], in which up- and down-spin species have non-degenerate Fermi surfaces. Here we demonstrate that magnetic quantum oscillation[14] measurements can provide a high-resolution, bulk-sensitive, three-dimensional (3D) mapping of the order parameter in an unconventional magnet. By rotating a magnetic field through high- and low-symmetry directions of the CrSb Brillouin zone, we show that the altermagnetic band structure of this material leads to a reduction of symmetry for each spin-split Fermi sheet away from nodal orientations. In momentum space, the exchange splitting between up and down spins follows the profile of the $\mathcal{Y}_4^{-3} = yz\,(3x^2 - y^2)$ real spherical harmonic—analogous to a *g*-orbital of the hydrogen atom. Although notoriously difficult to resolve in unconventional superconductors, our work demonstrates that the order parameter symmetry of unconventional magnets can be precisely mapped by quantum oscillatory quasiparticle spectroscopy, establishing CrSb as a prototypical *g*-wave metallic altermagnet.

There are two traditional types of collinear magnetic ordering: ferromagnetism[1,2], in which all spins point in the same direction, and antiferromagnetism[15], in which the spin polarization alternates up and down from site to site. In an antiferromagnet, the magnetic structure can be decomposed into two magnetic sublattices, resulting in a doubling of the magnetic unit cell[16] under translation. Recently, a third distinct classification was proposed, dubbed altermagnetism[9–13]. Like antiferromagnets, altermagnets possess alternating up- and down-spin orientations from site to site. However, the distinction is that in an altermagnet the spin sublattices are connected by rotational symmetries rather than just translation (or inversion). This leads to the lifting of Kramers spin degeneracy[17] and a momentum-dependent non-relativistic spin splitting of the electronic band structures[18]. Therefore, altermagnetism represents a distinct form of ordering, in which the momentum-dependent spin-split property of ferromagnets is combined with the spin-compensated zero net magnetization of antiferromagnets, opening new opportunities for magnetic memory and spintronic device applications[19].

Numerous altermagnet candidates have been identified from ab initio calculations[9,10,19–21], with experiments on MnTe giving good empirical correspondence with theoretical expectations[22–25]. However, although many semiconducting or insulating materials have been identified, only a handful of metallic altermagnet candidates have so far been proposed. The realization of a metallic altermagnet, with an ordering temperature far above 300 K, would be particularly desirable for efficient electronic transport in technological device settings[21].

Of metallic candidates, surface-sensitive photoemission spectra of RuO_2 (refs. 26,27), KV_2Se_2O (ref. 28) and CrSb (refs. 29–32) have been interpreted to show hallmarks of altermagnetic spin splitting. However, for the case of RuO_2, a variety of subsequent bulk-sensitive measurements[33–35] cast considerable doubt on whether this material is an altermagnet. Further photoemission studies[36,37] showed that this material seems to possess a topological surface state with Rashba-like spin splitting, which may give the appearance of altermagnetically lifted Kramers spin degeneracy although the bulk is actually nonmagnetic. A similar story has unfolded with KV_2Se_2O, for which the surface termination layer may be altermagnetic[38], yet neutron diffraction clearly resolves conventional antiferromagnetism throughout the bulk[39]. These cautionary tales motivate bulk-sensitive studies of candidate altermagnets, to firmly establish their intrinsic magnetic properties.

Nodal magnetic order parameters

We can frame our thinking of magnetic order parameter symmetries by analogy to unconventional superconductors. In a conventional *s*-wave BCS superconductor, the order parameter is the gap function $\Delta(\mathbf{k})$, which is an isotropic energy separation corresponding to a

[1]Cavendish Laboratory, University of Cambridge, Cambridge, UK. [2]National High Magnetic Field Laboratory, Tallahassee, FL, USA. [3]Hochfeld-Magnetlabor Dresden (HLD-EMFL), Helmholtz-Zentrum Dresden-Rossendorf, Dresden, Germany. [4]These authors contributed equally: Mengmeng Long, Theodore I. Weinberger, Zheyu Wu. ✉e-mail: tiw21@cam.ac.uk; alex.eaton@phy.cam.ac.uk

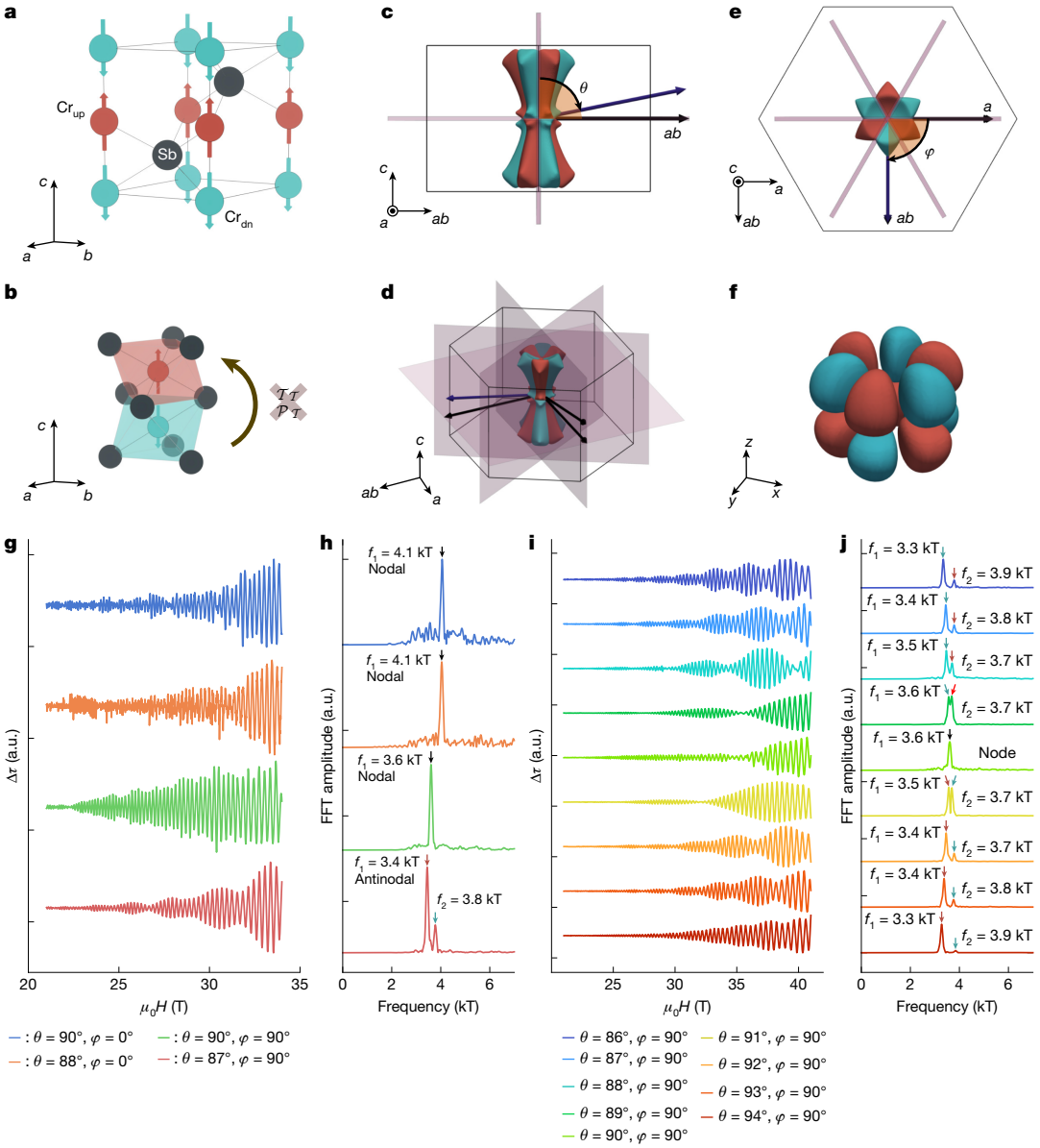


Fig. 1 | Nodal planes bisect *g*-wave-symmetric spin-split Fermi surface sheets in CrSb. a, The crystal structure of CrSb, with alternating magnetic moments on the Cr sites oriented along the *c*-axis. Red indicates spin-up and blue indictes spin-down. **b**, The trigonal arrangement of the antimony ions means that mapping a red chromium site to a blue one necessarily requires a screw rotation. **c**–**e**, The primary Fermi surface sheet of CrSb is a closed 3D ellipsoidal pocket, shaped like a dogbone. Nodal planes—where spin degeneracy is imposed by symmetry—are given by thin shaded slabs. The azimuthal angle φ is defined as the inclination from *a* to *ab* in the hexagonal basal plane; the polar angle θ is from *c* towards the basal *ab* plane. **f**, Visual depiction of the $\mathcal{Y}_4^{-3} = yz\,(3x^2 - y^2)$ real spherical harmonic, which characterizes the *g*-wave symmetry profile of altermagnetic spin splitting in CrSb. **g**,**h**, Quantum oscillations in the background-subtracted magnetic torque $\Delta\tau$ (**g**), rescaled to the same maximal amplitude and high-pass filtered for ease of presentation (see Methods for details) at magnetic field **H** orientations as indicated, and their FFT frequency spectra (**h**). A singular FFT peak is observed in the three nodal orientations, which splits into two peaks in the antinodal plane (coloured red). All measurements were performed at 0.4 K. **i**,**j**, $\Delta\tau$ and corresponding FFT spectra for small rotations of θ in the antinodal plane away from the *ab* direction towards ±*c*. For **H** aligned along *ab*, only one frequency is observed, which elsewhere splits into two distinct peaks, indicating altermagnetically spin-split Fermi sheets. a.u., arbitrary units.

dispersion possessing the same symmetries as the crystal. By contrast, unconventional superconductors[4] are those in which the pairing symmetry breaks crystal point group symmetries, or where the gap function exhibits a non-trivial phase structure (like a sign change) not required by the crystalline symmetry.

These concepts have recently been applied to magnetic systems[5,6]. Let us define the order parameter for an unconventional magnet as the exchange splitting (energy difference) between up- and down-spin states at a given wavevector, $\Delta(\mathbf{k}) = E(\mathbf{k}, \uparrow) - E(\mathbf{k}, \downarrow)$. This produces spin-split Fermi sheets separated by the (perpendicular) wavevector $k_\perp \simeq \Delta(\mathbf{k})/(\hbar v_F)$, where $v_F = \partial E/(\hbar \partial k)$ is the Fermi velocity. In this way, a ferromagnet is analogous to a BCS superconductor—its nonzero magnetization splits the Fermi surface into unequal majority and minority spin species, characterized by an isotropic energy gap between them. It follows that for an unconventional magnet of *p*-, *d*-, *f*- and *g*-wave symmetry, the Fermi surface will possess 1, 2, 3 and 4 highly symmetric nodal planes, respectively, at which up-character swaps to down, and vice versa.

CrSb crystallizes in the hexagonal $P6_3/mmc$ NiAs-type structure, with chromium atoms stacked along the crystallographic *c*-axis in octahedrally coordinated layers, whereas the antimony atoms fill the interstitial sites in a trigonal prismatic arrangement[40] (Fig. 1a,b). Below an

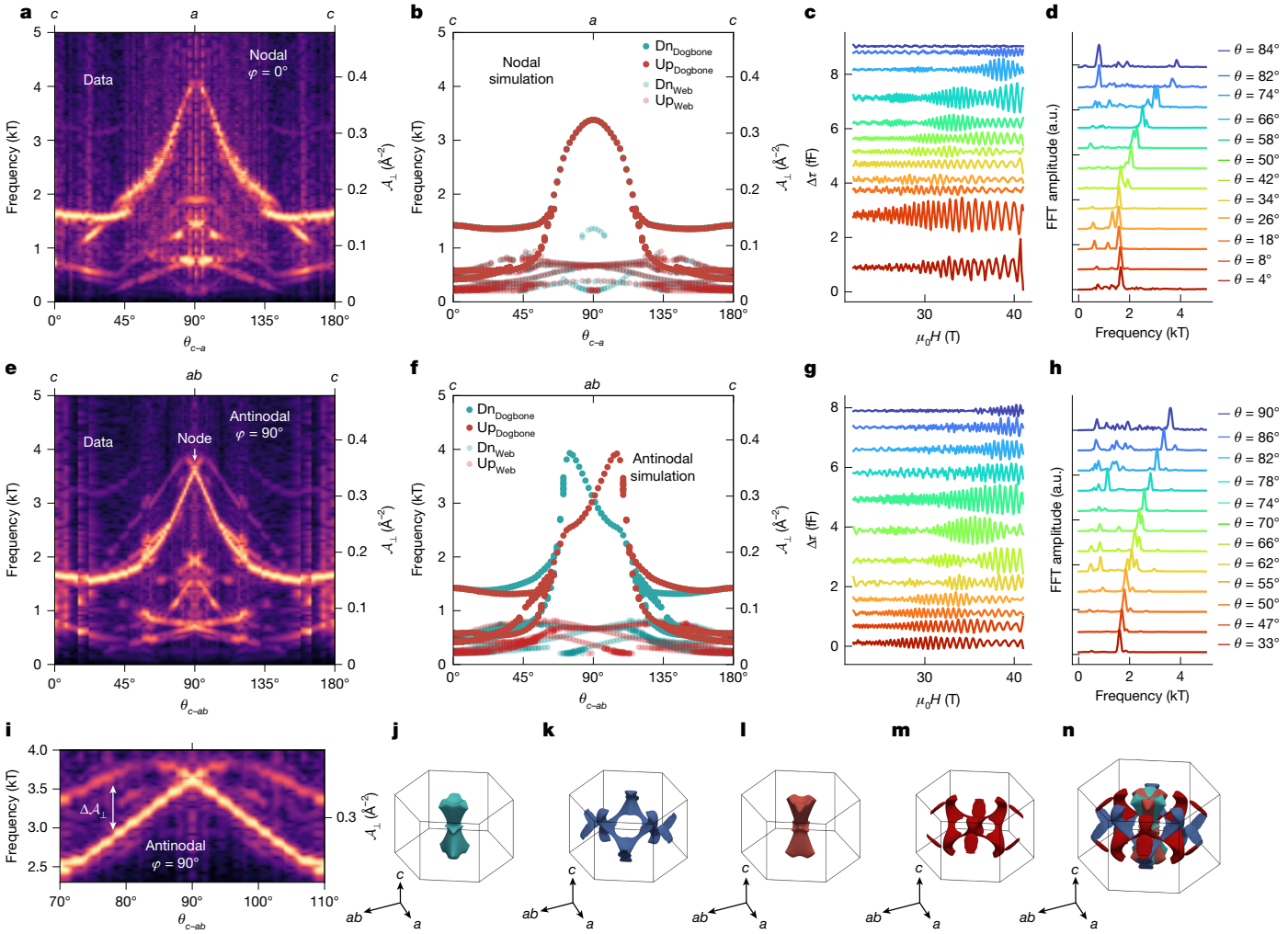


Fig. 2 | Mapping the altermagnetically spin-split Fermi surface of CrSb. **a**, Heatmap of the spectral intensity of quantum oscillatory frequencies compared with rotation angle in the nodal c–a plane. Brighter heatmap intensities correspond to larger quantum oscillatory amplitudes; data have been symmetrized through 90° for ease of presentation. **b**, Simulated frequency profile for the c–a plane from DFT calculations (see Methods and Supplementary Information). **c**,**d**, Selected $\Delta\tau$ curves and normalized FFTs that contributed to the heatmap in **a** (full dataset in Extended Data Fig. 2). All data were collected at 0.4 K. **e**–**h**, Data (**e**) and simulation (**f**) for the antinodal c–ab rotation plane, with waveforms and normalized FFTs in **g**,**h** (full dataset in Extended Data Fig. 3). Here, spin splitting between non-degenerate Fermi sheets is predicted by the simulation, which is clearly resolved experimentally close to $\theta = 90°$. **i**, Magnified view having high-pass filtered the raw data, to show the non-degenerate spin-up and spin-down frequency branches crossing the nodal plane at $\theta = 90°$, which are separated by about 1 kT. **j**–**m**, Fermi surface rendering of the spin-down sheets of the dogbone and web pockets (**j**,**k**) and their spin-up counterparts (**l**,**m**). **n**, The full Fermi surface of CrSb, including all spin-up and spin-down sheets. Additional renderings are given in Extended Data Fig. 6. a.u., arbitrary units.

ordering temperature of around 740 K (Extended Data Fig. 1), the chromium sites possess alternating magnetic moments oriented along the c-axis[41]. The trigonal arrangement of antimony necessarily requires a 6_3 screw rotation to map a spin-up chromium site to its spin-down counterpart. Consequently, although CrSb breaks both pure timereversal and primitive lattice-translation symmetries, it preserves a combined symmetry pairing this non-symmorphic spatial operation with time reversal. These symmetry properties motivate the proposal[10,13,21,32,42,43] that CrSb is a metallic altermagnet in which $\Delta(G\mathbf{k}) = -\Delta(\mathbf{k})$, where G is this composite operation.

Quantum oscillation measurements

In this work, we map the symmetry of $\Delta(\mathbf{k})$ in CrSb by performing magnetic quantum oscillation measurements through the de Haas–van Alphen effect[14,44], and show that this material is a g-wave altermagnet. Quantum oscillation experiments are an especially well-suited technique for resolving the nodal planes of an unconventional magnet, and hence the order parameter symmetry. This is because $\Delta(\mathbf{k})$ does not just go to zero for **k** on a nodal plane—it is also mirror-symmetric about the plane. Aligning a magnetic field within a nodal plane therefore produces quantum oscillation orbits for up- and down-spin Fermi sheets that are different, but can be mapped onto each other by a mirror operation about the nodal plane, and which therefore enclose the same area. This leads to a single quantum oscillation frequency per Fermi pocket for fields in nodal planes. By contrast, for fields oriented away from nodal planes, the up- and down-spin Fermi sheets are not related by any symmetry operation, and therefore typically enclose different areas, leading to two distinct quantum oscillation frequencies. This thereby yields an expected smoking-gun signature of altermagnetic spin splitting.

Throughout this article, we shall refer to rotations of the orientation of an applied magnetic field **H** through azimuthal angles φ defined in the crystallographic ab plane, and polar angles θ between c and the ab plane (Fig. 1c,e). Note that for hexagonal CrSb, the a direction is equivalent to b. The c–a plane is a highly symmetric nodal plane in which Kramers degeneracy is enforced by symmetry, whereas c–ab is antinodal, in which spin degeneracy is only symmetry-enforced at

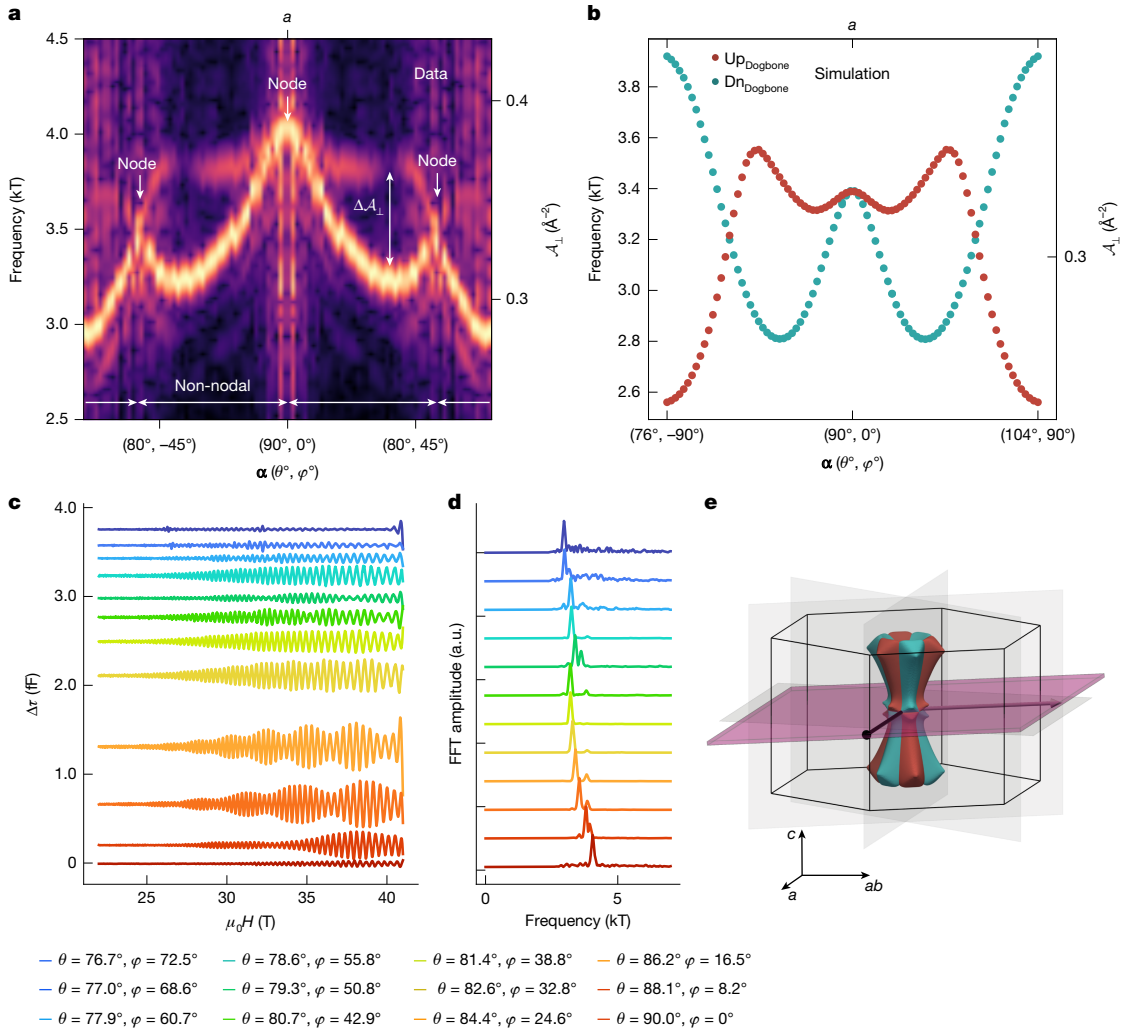


Fig. 3 | Confirmation of *g*-wave altermagnetic spin texture in CrSb. a, Heatmap of quantum oscillation frequencies compared with rotation angle (data have been symmetrized for ease of presentation). **b**, Simulated spin-up (red) and spin-down (blue) angular frequency profile computed by DFT. Here, we rotate **H** through a plane of low symmetry at a tilt of 14° from the *ab* plane, which is shown in Extended Data Fig. 4. We parameterize the orientation of **H** in the reference frame of the rotator mechanism by the angle within the rotation plane, α, which can be mapped back into the reference frame of the crystal by $\cos(\theta) = \sin(14°)\sin(\alpha)$ and $\tan(\varphi) = \cos(14°)\tan(\alpha)$. Symmetry-enforced nodal planes are crossed at $\varphi = 0°$ and at $\varphi = \pm 60°$. At all other orientations in this low-symmetry plane, significant spin splitting is expected by DFT and observed experimentally. **c**,**d**, Selected $\Delta\tau$ curves and corresponding FFTs that contributed to the heatplot in **a** (full dataset in Extended Data Fig. 5). **e**, The tilted rotation plane through which **H** was swept and in which the arc that is traced out crosses a nodal plane every 60° increment of φ, because of the *g*-wave symmetry profile. a.u., arbitrary units.

c and *ab*. In CrSb, *g*-wave splitting should result in nodal planes every $\delta\varphi = 60°$ for rotations in the *a*–*ab* plane, and every $\delta\theta = 90°$ rotating through the *c*–*ab* plane.

We present the experimentally deduced central Fermi surface pocket of CrSb, with its high-symmetry nodal planes between up and down sheets, in Fig. 1c–f. This sheet is a closed ellipsoid-like pocket of hole character, shaped like a dogbone. In Fig. 1g, we plot background-subtracted magnetic torque $\Delta\tau$ as a function of H, to focus on the oscillatory component, measured by cantilever beam magnetometry (Methods). The blue waveform was measured for $\mathbf{H} \parallel a$ at $\theta = 90°$, $\varphi = 0°$, with the orange data collected a small rotation away in the *c*–*a* plane to $\theta = 88°$, $\varphi = 0°$. The corresponding fast Fourier transform (FFT) spectra in Fig. 1h for both of these orientations exhibit a singular frequency peak at 4.1 kT.

Tracking $\Delta(\mathbf{k}) = E(\mathbf{k}, \uparrow) - E(\mathbf{k}, \downarrow)$

Let us now contrast this with the case of fields in the *c*–*ab* (antinodal) plane. The green curve of Fig. 1g was obtained for $\mathbf{H} \parallel ab$ (that is, $\theta = 90°$, $\varphi = 90°$), with a monofrequency profile of 3.6 kT. On a small θ rotation of 3° towards *c*, a distinct beat pattern emerges (red curve), with two peaks clearly resolved in the frequency spectra. This is characteristic of the Fermi surface becoming spin-split into two non-degenerate sheets—one spin-up and the other spin-down.

Figure 1i,j tracks this split peak structure for fields close to the *ab* direction. Incrementing θ in 1° steps through the *c*–*ab* plane, we find that the singular on-axis peak of 3.6 kT clearly splits into two distinct frequency branches, which by 4° of rotation are separated by 0.6 kT. This is reflected in the profile of the waveforms themselves, which exhibit a pronounced beat structure that is acutely sensitive to θ.

The full angular profiles of quantum oscillation frequency spectra for the *c*–*a* (nodal) and *c*–*ab* (antinodal) planes are shown in Fig. 2. Quantum oscillation frequencies are directly proportional to the Fermi surface cross-sectional area $\mathcal{A}_\perp$ normal to **H** (refs. 45,46). We compare with simulated quantum oscillation frequency spectra from density functional theory (DFT) calculations (see Methods for details). The dogbone pocket exhibits quantum oscillation frequencies of 4.1 kT for $\mathbf{H} \parallel a$ and 3.6 kT for $\mathbf{H} \parallel ab$. Two other bands of electron character also

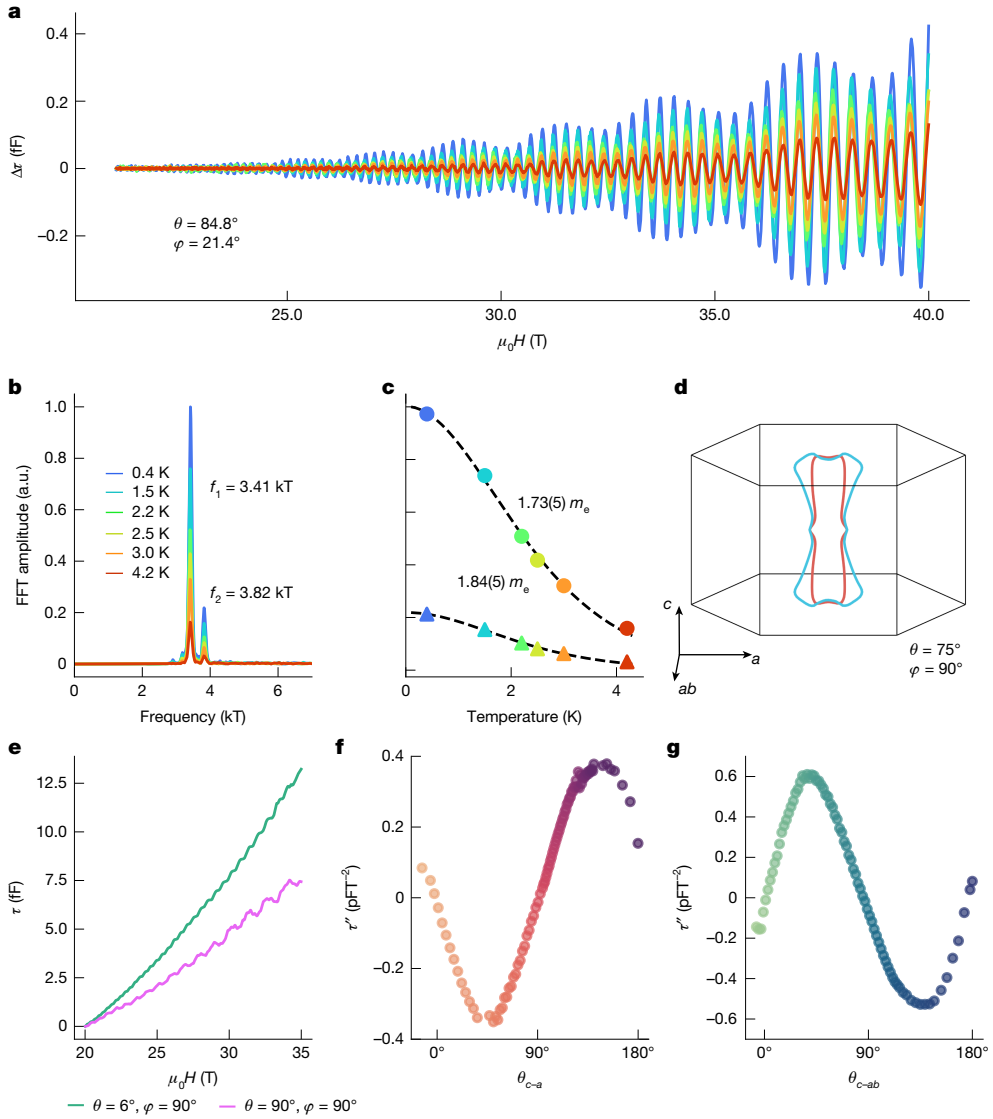


Fig. 4 | Spin-split effective mass study. a, Quantum oscillations at incremental temperatures for $\theta = 84.8°$, $\varphi = 21.4°$. **b**, The corresponding frequency spectra, with temperatures indicated. $\Delta\tau$ was high-pass filtered to focus on two frequency components, at $f_1 = 3.41$ kT and $f_2 = 3.82$ kT (Methods), which come from spin-split up and down sheets of the dogbone pocket. See Extended Data Fig. 9 for additional data. **c**, Temperature dependence of quantum oscillation amplitude fitted to the Lifshitz–Kosevich formula[46], yielding effective cyclotron masses of $m_1^* = 1.73(5)m_e$ and $m_2^* = 1.84(5)m_e$. The ratio of $\sqrt{f_1/f_2}$ is equal to that of m_1^*/m_2^*, as expected for these two frequency components being two spin-split daughters of the same mother Fermi sheet. **d**, Visualization of spin-up and spin-down orbits around the dogbone cross-section, which can enclose markedly different areas for the same field orientation. See Extended Data Fig. 8 for further comparisons. **e**, Raw torque τ without background subtraction at two orientations as indicated. Close to high symmetry, the overall cantilever deflection is small, hence τ is dominated by the oscillatory component of magnetization. The raw torque for $\theta = \varphi = 90°$ has been scaled by a factor of 5 so that its magnitude is comparable to that at $\theta = 6°$, $\varphi = 90°$. **f**,**g**, Second derivative of torque with respect to field, τ'', for rotations in the nodal c–a plane (**f**) and in the antinodal c–ab plane (**g**). Although the quantum oscillation frequency profiles for these two planes are markedly different, with the loss of mirror symmetry for each spin-split frequency trace in the antinodal plane (Fig. 2e), the background torque profile still exhibits the higher symmetry representative of the crystal structure. a.u., arbitrary units.

cross the Fermi level, leading to another more geometrically complex Fermi sheet with a web-like shape (Fig. 2). The web sheet produces a very complicated dependence of quantum oscillation frequency on angle in the low-frequency range $\lesssim$2 kT. Away from nodal planes, the web is also split into up and down sheets, but its geometrical complexity makes this more difficult to resolve than for the dogbone. We therefore predominantly focus on the dogbone for **H** oriented close to a or to ab, which produces quantum oscillation orbits with frequencies $\gtrapprox$3 kT, well above those from the web.

Symmetry-enforced spin degeneracy causes the quantum oscillation frequencies from both the spin-up and spin-down Fermi sheets to be equivalent for fields in the nodal c–a plane, as shown by our simulation (Fig. 2b). By contrast, for fields in the antinodal c–ab plane, a large frequency splitting should occur over the approximate angular interval $60° < \theta < 120°$ (Fig. 2e,f), before the geometric profile of the dogbone leads to an accidental degeneracy. This is exactly what we observed in Fig. 1i,j and is clearly visible in the spectral intensity near $\theta = 90°$ in Fig. 2e. In Fig. 2i, we present a magnification of this region to focus on this spectral range. The overlap of frequencies at $\mathbf{H} \parallel ab$, which is abruptly split on incrementing θ, is characteristic of the altermagnetic lifting of spin degeneracy, producing two spin-split Fermi sheets. Notably, whereas in the nodal plane both spin-up and spin-down frequency traces are expected to repeat every 90°, in the antinodal plane this reduces to every 180°—exactly as observed experimentally.

To trace out the spin splitting of the CrSb Fermi surface away from its nodal planes, we measured quantum oscillations in a tilted plane of rotation, chosen such that an arc of low symmetry connects two symmetry-enforced nodal orientations. Along this arc, the spin splitting should be considerable, but collapse to yield monofrequency waveforms at nodal orientations. We experimentally performed this by first rotating the sample platform 14° orthogonally to the axis of the solenoid before loading it into the magnet. Then, we rotated in situ through a polar angle (labelled α in Fig. 3), about an axis orthogonal to **H**, but always at a tilt of 14° relative to the sample holder. This setup means that **H** may still be oriented along a, but subsequent rotation of the sample holder increments θ (c–a) and φ (a–ab) such that $\cos(\theta) = \sin(14°)\sin(\alpha)$ and $\tan(\varphi) = \cos(14°)\tan(\alpha)$ (see Extended Data Fig. 4 for further details). We plot the resulting data for these rotational measurements in Fig. 3, including the simulated up- and down-sheet frequency profiles computed from DFT.

The correspondence between experimental observation (Fig. 3a) and theoretical prediction (Fig. 3b) is very good. A singular frequency peak is observed for $\mathbf{H} \parallel a$ ($\theta = 90°$, $\varphi = 0°$) in Fig. 3d, giving a bright spot at the nodal location of $\varphi = 0°$ in Fig. 3a. On incrementing α, this then splits into two distinct branches, which, within resolution, come back together again close to $\varphi = \pm 60°$ as the next nodal plane is crossed, as expected for $\Delta(\mathbf{k})$ possessing g-wave symmetry.

Altermagnetic scaling of $m^*_\uparrow/m^*_\downarrow = \sqrt{f_\uparrow/f_\downarrow}$

We determined the effective cyclotron masses of the two spin-split surfaces in a Lifshitz–Kosevich temperature-dependence study of quantum oscillation amplitude in this rotation plane at $\alpha = 22°$, which in the crystal reference frame corresponds to **H** aligned at $\theta = 84.8°$, $\varphi = 21.4°$ (Fig. 4a). Two peaks are resolved, with $f_1 = 3.41$ kT and $f_2 = 3.82$ kT. Fitting the temperature-dependent oscillatory damping to Lifshitz–Kosevich theory[46] yields effective masses $m_1^* = 1.73(5)m_e$ and $m_2^* = 1.84(5)m_e$, where m_e is the bare electron mass. For two quantum oscillation frequency branches that are spin-split daughters of the same mother sheet, the daughters are expected to share the same mass renormalization factors and Fermi velocity profile. The quantum oscillation mass is given by $m^* = (\partial\mathcal{A}_\parallel/\partial E)\hbar^2/(2\pi)$, where $\partial\mathcal{A}_\parallel/\partial E = (\partial\mathcal{A}_\parallel/\partial k)/(\hbar v_F)$. If the orbit area scales with the square of the orbit size, $(\partial\mathcal{A}_\parallel/\partial k) \propto \sqrt{\mathcal{A}_\parallel}$, with $\mathcal{A}_\parallel$ in turn proportional to the associated quantum oscillation frequency. If $v_F(k)$ is the same around the two orbits, we would therefore expect $m_1^*/m_2^* = \sqrt{f_1/f_2}$. This is what we observe: $m_1^*/m_2^* = 0.94 \pm 0.04 \simeq \sqrt{f_1/f_2} = 0.945$. This result provides strong corroboration that these two frequencies may therefore be attributed to altermagnetic spin splitting of the same parent sheet. The maximum spin splitting can likewise be estimated from the frequency difference $\delta f = f_2 - f_1 = 0.41$ kT, which according to the Onsager relation[45] translates to a difference between the areas enclosed by spin-up and spin-down orbits as $\delta\mathcal{A} = \delta f(2\pi e)/\hbar = \Delta\partial\mathcal{A}/\partial\varepsilon = m^*\Delta(2\pi/\hbar^2)$, with Δ the energy splitting at the Fermi level. With the observed average effective mass $m^* \simeq 2.03m_e$, we thereby estimate a spin splitting at the Fermi level of $\Delta \approx 25$ meV for this field orientation.

g-Wave magnetic order parameter

Putting together our results from the three different rotation planes presented in Figs. 2 and 3, we can firmly pin down the unconventional magnetic order parameter symmetry of CrSb. By tracking how the spin-split quantum oscillation frequency profile of the primary CrSb Fermi pocket evolves under rotation, we identify four nodal planes in total: three defined for all θ at $\varphi = 0°$, 60° and 120°, and one for all φ at $\theta = 90°$. We can therefore compare the symmetry of our unconventional magnetic order parameter, $\Delta(\theta, \varphi)$, to that of a real spherical harmonic. We find that $\Delta(\theta, \varphi)$ obeys the symmetries of $\mathcal{Y}_4^{-3}(\theta, \varphi) \propto P_4^3(\cos\theta)\sin 3\varphi$ defined in terms of the associated Legendre polynomial $P_\ell^m(x)$ (ref. 47) (Methods). This harmonic transforms as the B_{1g} irreducible representation of the D_{6h} point group of CrSb. $\mathcal{Y}_4^{-3}(\theta, \varphi)$ can be expressed in Cartesian form as $yz(3x^2 - y^2)$ or equivalently in spherical polars as $r^4\sin^3(\theta)\cos(\theta)\sin(3\varphi)$ (Fig. 1f). This function has nodes when $\theta = 0°, 90°$ and $\varphi = 0°, 60°, 120°$, just as $\Delta(\theta, \varphi)$ does. Our study thereby demonstrates the sensitivity of quantum oscillation measurements to spin-split band structures, positioning these measurements as an ideally suited diagnostic tool for ascertaining the order parameter symmetry of unconventional metallic magnets.

In summary, our systematic bulk-sensitive quantum oscillation measurements have mapped out the unconventional magnetic order parameter symmetry of CrSb, revealing the g-wave altermagnetic spin texture. This manifests in the k-dependence of the spin splitting per Fermi pocket, $\Delta(\mathbf{k})$. For magnetic fields applied in highly symmetric nodal planes, $\Delta(\mathbf{k})$ is always zero—whereas, rotating through arcs of low symmetry $\Delta(\mathbf{k})$ is generally large and well-resolvable, collapsing back to zero on crossing through a nodal plane. For fields applied in nodal planes, quasiparticle orbits are spin-degenerate and mirror-symmetric. By contrast, in antinodal planes, this mirror symmetry is lost, leading to spin-split quantum oscillation frequency traces—providing a hallmark signature of altermagnetic ordering. Furthermore, we observe excellent quantitative agreement in the ratios between quantum oscillatory frequencies and effective masses, as theoretically expected for spin-split Fermi surface sheets. In combination, these results provide strong empirical evidence supporting the designation of CrSb as a room-temperature metallic altermagnet. Furthermore, our optimized growth procedure has produced high-quality crystals with residual resistivities as low as 2 μΩ cm. Given that CrSb is relatively insensitive to air and moisture, it can be synthesized to high purity, the altermagnetic ordering temperature is very high, and both chromium and antimony are relatively abundant easily sourced elements, this combination of favourable properties positions CrSb as a leading material for pursuing applications in next-generation low-energy spintronic devices.

Online content

Any methods, additional references, Nature Portfolio reporting summaries, source data, extended data, supplementary information, acknowledgements, peer review information; details of author contributions and competing interests; and statements of data and code availability are available at https://doi.org/10.1038/s41586-026-10902-z.

1. Curie, P. *Propriétés magnétiques des corps à diverses températures* (Gauthier-Villers, 1895).
2. Heisenberg, W. Zur Theorie des Ferromagnetismus. *Z. Phys.* **49**, 619–636 (1928).
3. Bardeen, J., Cooper, L. N. & Schrieffer, J. R. Theory of superconductivity. *Phys. Rev.* **108**, 1175–1204 (1957).
4. Stewart, G. R. Unconventional superconductivity. *Adv. Phys.* **66**, 75–196 (2017).
5. Jungwirth, T., Fernandes, R. M., Sinova, J. & Smejkal, L. Altermagnets and beyond: nodal magnetically-ordered phases. Preprint at arxiv.org/abs/2409.10034 (2024).
6. Liu, Q., Dai, X. & Blügel, S. Different facets of unconventional magnetism. *Nat. Phys.* **21**, 329–331 (2025).
7. Song, Q. et al. Electrical switching of a *p*-wave magnet. *Nature* **642**, 64–70 (2025).
8. Yamada, R. et al. A metallic *p*-wave magnet with commensurate spin helix. *Nature* **646**, 837–842 (2025).
9. Šmejkal, L., Sinova, J. & Jungwirth, T. Beyond conventional ferromagnetism and antiferromagnetism: a phase with nonrelativistic spin and crystal rotation symmetry. *Phys. Rev. X* **12**, 031042 (2022).
10. Šmejkal, L., Sinova, J. & Jungwirth, T. Emerging research landscape of altermagnetism. *Phys. Rev. X* **12**, 040501 (2022).
11. Hayami, S., Yanagi, Y. & Kusunose, H. Momentum-dependent spin splitting by collinear antiferromagnetic ordering. *J. Phys. Soc. Jpn.* **88**, 123702 (2019).
12. Šmejkal, L., González-Hernández, R., Jungwirth, T. & Sinova, J. Crystal time-reversal symmetry breaking and spontaneous Hall effect in collinear antiferromagnets. *Sci. Adv.* **6**, eaaz8809 (2020).
13. Ma, H.-Y. et al. Multifunctional antiferromagnetic materials with giant piezomagnetism and noncollinear spin current. *Nat. Commun.* **12**, 2846 (2021).
14. Shoenberg, D. *Magnetic Oscillations in Metals* (Cambridge Univ. Press, 1984).
15. Néel, L. Influence des fluctuations du champ moléculaire sur les propriétés magnétiques des corps. *Ann. Phys.* **10**, 5–105 (1932).
16. Shull, C. G. & Smart, J. S. Detection of antiferromagnetism by neutron diffraction. *Phys. Rev.* **76**, 1256–1257 (1949).

17. Kramers, H. A. Théorie générale de la rotation paramagnétique dans les cristaux. *Proc. Acad. Amsterdam* **33**, 959–972 (1930).
18. Jungwirth, T. et al. Altermagnetism: an unconventional spin-ordered phase of matter. *Newton* **1**, 100162 (2025).
19. Song, C. Altermagnets as a new class of functional materials. *Nat. Rev. Mater.* **10**, 473–485 (2025).
20. Fender, S. S., Gonzalez, O. & Bediako, D. K. Altermagnetism: a chemical perspective. *J. Am. Chem. Soc.* **147**, 2257–2274 (2025).
21. Wan, X., Mandal, S., Guo, Y. & Haule, K. High-throughput search for metallic altermagnets by embedded dynamical mean field theory. *Phys. Rev. Lett.* **135**, 106501 (2025).
22. Krempaský, J. et al. Altermagnetic lifting of Kramers spin degeneracy. *Nature* **626**, 517–522 (2024).
23. Lee, S. et al. Broken Kramers degeneracy in altermagnetic MnTe. *Phys. Rev. Lett.* **132**, 036702 (2024).
24. Osumi, T. et al. Observation of a giant band splitting in altermagnetic MnTe. *Phys. Rev. B* **109**, 115102 (2024).
25. Amin, O. J. et al. Nanoscale imaging and control of altermagnetism in MnTe. *Nature* **636**, 348–353 (2024).
26. Fedchenko, O. et al. Observation of time-reversal symmetry breaking in the band structure of altermagnetic RuO_2. *Sci. Adv.* **10**, eadj4883 (2024).
27. Lin, Z. et al. Observation of giant spin splitting and d-wave spin texture in room temperature altermagnet RuO_2. Preprint at arxiv.org/abs/2402.04995 (2024).
28. Jiang, B. et al. A metallic room-temperature d-wave altermagnet. *Nat. Phys.* **21**, 754–759 (2025).
29. Reimers, S. et al. Direct observation of altermagnetic band splitting in CrSb thin films. *Nat. Commun.* **15**, 2116 (2024).
30. Ding, J. et al. Large band splitting in *g*-wave altermagnet CrSb. *Phys. Rev. Lett.* **133**, 206401 (2024).
31. Zeng, M. et al. Observation of spin splitting in room-temperature metallic antiferromagnet CrSb. *Adv. Sci.* **11**, 2406529 (2024).
32. Yang, G. et al. Three-dimensional mapping of the altermagnetic spin splitting in CrSb. *Nat. Commun.* **16**, 1442 (2025).
33. Hiraishi, M. et al. Nonmagnetic ground state in RuO_2 revealed by muon spin rotation. *Phys. Rev. Lett.* **132**, 166702 (2024).
34. Keßler, P. et al. Absence of magnetic order in RuO_2: insights from μSR spectroscopy and neutron diffraction. *npj Spintronics* **2**, 50 (2024).
35. Wu, Z. et al. Fermi surface of RuO_2 measured by quantum oscillations. *Phys. Rev. X* **15**, 031044 (2025).
36. Liu, J. et al. Absence of altermagnetic spin splitting character in rutile oxide RuO_2. *Phys. Rev. Lett.* **133**, 176401 (2024).
37. Osumi, T. et al. Spin-degenerate bulk bands and topological surface states associated with Dirac nodal lines in RuO_2. *Phys. Rev. B* **113**, 085116 (2026).
38. Lange, C. et al. Emergent altermagnetism at surfaces of antiferromagnets: full symmetry classification and material identification. Preprint at arxiv.org/abs/2602.08773 (2026).
39. Sun, Y. et al. Antiferromagnetic structure of KV_2Se_2O: a neutron diffraction study. *Phys. Rev. B* **112**, 184416 (2025).
40. Willis, B. T. M. Crystal structure and antiferromagnetism of CrSb. *Acta Crystallogr.* **6**, 425–426 (1953).
41. Snow, A. I. Neutron diffraction investigation of the atomic magnetic moment orientation in the antiferromagnetic compound CrSb. *Phys. Rev.* **85**, 365–365 (1952).
42. Biniskos, N. et al. Systematic mapping of altermagnetic magnons by resonant inelastic X-ray circular dichroism. *Nat. Commun.* **16**, 9311 (2025).
43. Singh, A. K. et al. Chiral spin-split magnons in the metallic altermagnet CrSb. Preprint at https://arxiv.org/abs/2511.16086 (2025).
44. de Haas, W. J. & van Alphen, P. M. The dependence of the susceptibility of diamagnetic metals upon the field. *Proc. Akad. Amsterdam* **130**, 1106–1118 (1930).
45. Onsager, L. Interpretation of the de Haas-van Alphen effect. *Philos. Mag.* **43**, 1006–1008 (1952).
46. Lifshitz, I. M. & Kosevich, A. M. Theory of magnetic susceptibility in metals at low temperatures. *Sov. Phys. JETP* **2**, 636–645 (1956).
47. Blanco, M. A., Flórez, M. & Bermejo, M. Evaluation of the rotation matrices in the basis of real spherical harmonics. *J. Mol. Struct. Theochem.* **419**, 19–27 (1997).

Publisher's note Springer Nature remains neutral with regard to jurisdictional claims in published maps and institutional affiliations.

Open Access This article is licensed under a Creative Commons Attribution 4.0 International License, which permits use, sharing, adaptation, distribution and reproduction in any medium or format, as long as you give appropriate credit to the original author(s) and the source, provide a link to the Creative Commons licence, and indicate if changes were made. The images or other third party material in this article are included in the article's Creative Commons licence, unless indicated otherwise in a credit line to the material. If material is not included in the article's Creative Commons licence and your intended use is not permitted by statutory regulation or exceeds the permitted use, you will need to obtain permission directly from the copyright holder. To view a copy of this licence, visit http://creativecommons.org/licenses/by/4.0/.

© The Author(s) 2026

Methods

Crystal growth

Single-crystal CrSb specimens were grown by the chemical vapour transport technique. Stoichiometric amounts of Cr (chunks, 99.995%) and Sb (Shots, 99.9999%) were used as source material. Iodine was added as a transport agent, calculated to have a pressure of 1 bar at growth conditions. The starting materials were sealed under vacuum in a quartz ampoule and placed in a horizontal two-zone furnace. The temperature was slowly ramped up to T_1 = 925 °C and T_2 = 900 °C, left for 2 weeks, and subsequently cooled at the furnace cooling rate to room temperature. The resulting crystals were hexagonal platelets up to 1.5 mm in diameter, along with larger areas possessing intergrown crystals of CrSb, several mm in size. Only single-crystal specimens were used in this study.

Sample characterization

Several crystals were picked from a batch of single crystals and crushed into a fine powder. This powdered sample was then distributed on a microscope slide, which had a thin layer of vacuum grease. Powder X-ray diffraction was measured in the Bragg–Brentano geometry on a Bruker D8, using a Cu source, with the results plotted in Extended Data Fig. 1. The measurement was performed in a 2θ range of 10°–90°, with no peaks observed below 20°.

The obtained data display sharp, well-defined peaks, indicating a high level of crystallinity. The data were analysed using the Rietveld method, yielding an excellent fit (R_{Bragg} = 3.39), which describes all observed peaks, thereby indicating that the samples are phase pure. The measured crystal structure is in good agreement with previous studies[40].

We also performed electrical transport, magnetization and Laue diffractometry measurements (Extended Data Fig. 1). Samples were predominantly screened by temperature-dependent resistivity measurements, used to extract their residual resistivity ratios (RRRs). To do this, we fitted the low-temperature data to the square of the temperature and extrapolated to absolute zero to determine the residual resistivity. The 300 K resistivity was then divided by this value to yield the RRR. Higher RRR values indicate longer mean free paths and hence higher crystalline quality. Typical RRR values were in the approximate range of 10–28. High-quality specimens were then oriented by Laue diffractometry, in preparation for high magnetic field de Haas–van Alphen (dHvA) effect measurements.

dHvA effect torque magnetometry measurements

High-quality samples were selected following characterization screening and brought to the National High Magnetic Field Laboratory, Tallahassee, Florida. For torque magnetometry measurements, we largely followed the methodology outlined in ref. 48. Samples were mounted on flexible BeCu cantilevers and affixed using multiple layers of General Electric low-temperature varnish, giving good thermal contact and strong adhesion between sample and cantilever. Cantilevers were soldered in place, such that the cantilever head was suspended above a copper baseplate by a short separation distance. As the magnetic field was swept, the change in capacitance between the cantilever and baseplate, due to the magnetic torque exerted on the sample, was measured by a General Radio analogue capacitance bridge using phase-sensitive detection. The change in torque was calibrated to units of farads using an Andeen-Hagerling digital capacitance bridge.

All dHvA measurements were performed in the 41.5 T all-resistive magnet in Tallahassee. A ^{3}He sample environment was used, along with a probe mounting of our custom design. Rotations of the sample orientation with respect to the magnetic field were performed in situ using a brushless linear motor. Angles were calibrated by the change in sign of the torque background—identifying high-symmetry directions of the crystal—and verified using a Hall sensor.

The oscillatory component $\Delta\tau$ was isolated from the background magnetic torque τ by performing a locally estimated scatterplot smoothing (LOESS)[49] subtraction. In general, owing to the intricate web sheet of the CrSb Fermi surface, the dHvA waveform at a given angle could be quite complicated because of the presence of numerous frequency components. To simplify our analysis and concentrate on the dogbone Fermi sheet, we often performed combined high-pass filtering with short LOESS windows in our analysis. The dogbone frequencies are most prominent above 3 kT, and so we performed Butterworth high-pass filtering of frequencies in inverse field in this range. This was combined with a short sliding LOESS window over τ, which effectively fits any slow oscillations within the background (assumed to be quadratic in H), therefore producing a $\Delta\tau$ waveform dominated by higher-frequency components. For the $\Delta\tau$ traces presented in Fig. 1, this involved using a LOESS window of 0.7 T. In Fig. 2, we used a window of length 1.2 T to show the strong spectral weight at lower frequencies due to the web. By contrast, in Fig. 4, we used a window of only 0.6 T to focus on the >3 kT components in our temperature-dependence study.

DFT calculations

DFT calculations for CrSb were performed using the all-electron, full-potential linearized augmented plane-wave (FP-LAPW) method as implemented in the WIEN2k code[50]. The electronic structure was converged on a 43 × 43 × 28 Monkhorst–Pack k-point mesh within the Brillouin zone of the primitive hexagonal unit cell. Exchange–correlation effects were treated within the generalized gradient approximation. We specified two distinct Cr sites (Cr_1 and Cr_2) within the primitive unit cell, corresponding to Cr atoms adopting up and down spin polarization. Calculations were initialized so that one Cr site has a higher spin-up density and the other has a spin-down density. The onsite spin polarization was then allowed to vary throughout the self-consistency cycles until the compensated collinear ground state was reached. Quantum oscillation frequency analysis of the resultant Fermi surface sheets was determined using SKEAF (ref. 51). Fermi surface visualization was performed using py_FS (refs. 48,52).

We assumed that ambient-pressure CrSb in the NiAs-type structure ($P6_3/mmc$) adopts lattice parameters a = 4.12 Å, b = 4.12 Å and c = 5.47 Å. Within the unit cell, there are two equivalent Cr sites and two equivalent Sb sites, as specified by Extended Data Table 1. We reduce the symmetry of the crystal lattice from $P6_3/mmc$ to $P3m1$ by specifying that the two Cr sites adopt opposite spins.

DFT calculations converge on a Fermi surface, in which the bands associated with the down and up 'dogbone' surfaces are open about the high-symmetry point, corresponding to a cylindrical topology. This is inconsistent with our quantum oscillation measurements, in which we resolve oscillations from these sheets for magnetic fields very close to the a and ab directions. No frequencies would be observed for these field orientations if the sheets were cylindrical. Therefore, we propose that these bands form closed Fermi surface sheets with dogbone-like geometry. To 'close' the open Fermi surface sheets of our DFT calculations, we shift our band edges relative to the Fermi energy. The dogbone-like sheets were shifted down by 0.11 eV so that the calculated frequencies along the a, ab and c directions are in good agreement with the quantum oscillation data. As the dogbone sheets are of hole character, we shifted up the 'web' sheets (of electron character) by 0.015 eV to keep the total carrier number constant (see Supplementary Information).

Consideration of spin–orbit coupling

Real materials always exhibit some spin–orbit coupling and many-body electronic correlations, meaning a purely non-relativistic framework is only ever an idealization. Nevertheless, our symmetry-based interpretation remains robust. Because CrSb possesses an inversion-symmetric crystal structure, the spatial symmetries protecting the orientation of the nodal planes remain intact. Furthermore, under the intense magnetic fields used in our experiments, field-assisted tunnelling (magnetic breakdown) allows quasiparticles to traverse small hybridization gaps

opened by weak spin–orbit coupling, effectively restoring the pristine altermagnetic trajectories. As detailed in the Supplementary Information (in which we also explicitly account for electronic correlations), these considerations justify our simplified symmetry picture introduced here, yielding a direct mapping between the quantum oscillation frequency spectra and the underlying altermagnetic order parameter $\Delta\mathbf{k}$.

Energy splitting from quantum oscillation frequencies

From the Onsager relation[45], we can equate a quantum oscillation frequency to a reciprocal space area as

$$f(E) = \frac{\hbar}{2\pi e}\mathcal{A}(E). \tag{1}$$

The cyclotron mass of an orbit, m^*, is related to the rate of change of the orbital area by

$$m^* = \frac{\hbar^2}{2\pi}\frac{\partial \mathcal{A}}{\partial E}\bigg|_{E_F}. \tag{2}$$

By taking the derivative of equation (1) with respect to E, we then determine

$$\frac{\mathrm{d}f}{\mathrm{d}E} = \frac{\hbar}{2\pi e}\frac{\partial \mathcal{A}}{\partial E} = \frac{\hbar}{2\pi e}\frac{2\pi}{\hbar^2}m^* = \frac{m^*}{e\hbar}. \tag{3}$$

We can use this to determine the energy difference associated with the frequency splitting of two bands:

$$\Delta E \sim \Delta f\frac{\mathrm{d}E}{\mathrm{d}f} = \frac{e\hbar}{m^*}\Delta f. \tag{4}$$

Spherical harmonic notation

In the text, we represent the symmetry of the altermagnetic spin splitting of CrSb in terms of the real spherical harmonic $\mathcal{Y}_4^{-3}(\theta,\varphi)$.

The complex spherical harmonics can be defined in terms of the associated Legendre polynomials as $Y_\ell^m(\theta,\varphi) = N_{\ell m}\mathrm{e}^{\mathrm{i}m\varphi}P_\ell^m(\cos\theta)$, where $N_{\ell m}$ is a normalization factor, $P_\ell^m(x)$ is an associated Legendre polynomial, and $Y_\ell^m(\theta,\varphi)$ is the complex spherical harmonic for $\ell \geq 0$ and $m \in [-\ell, \ell]$. The complex spherical harmonics are eigenfunctions of the total angular momentum operator $\hat{L}^2$ and of the generator of rotations about the azimuthal axis $\hat{L}_z$, spanning a complete orthonormal basis.

The complex spherical harmonics are defined up to a phase factor $\mathrm{e}^{\mathrm{i}m\varphi}$, and so their magnitude does not change as a function of φ. Therefore, it is convenient to work in the basis of the real spherical harmonics, which have explicit φ dependence, when describing the symmetry of an unconventional magnetic order parameter. We can define the real spherical harmonics $\mathcal{Y}_\ell^m(\theta,\varphi)$ in terms of linear combinations of complex harmonics according to

$$\mathcal{Y}_\ell^m = \begin{cases} \frac{1}{\sqrt{2}}(Y_\ell^{-m} + (-1)^m Y_\ell^m) & \text{if } m > 0 \\ Y_\ell^0 & \text{if } m = 0 \\ \frac{\mathrm{i}}{\sqrt{2}}(Y_\ell^{-|m|} - (-1)^{|m|} Y_\ell^{|m|}) & \text{if } m < 0, \end{cases} \tag{5}$$

or, equivalently, in terms of the associated Legendre polynomials

$$\mathcal{Y}_\ell^m = \begin{cases} \sqrt{2}(-1)^m N_{\ell m} P_\ell^m(\cos\theta)\cos(m\varphi) & \text{if } m > 0 \\ N_{\ell 0} P_\ell^0(\cos\theta) & \text{if } m = 0 \\ \sqrt{2}(-1)^m N_{\ell |m|} P_\ell^{|m|}(\cos\theta)\sin(|m|\varphi) & \text{if } m < 0. \end{cases} \tag{6}$$

Defining the real spherical harmonics this way means they form a complete set that spans the same basis as the complex spherical harmonics; however, importantly, they have well-defined varying magnitudes as a function of φ. This allows us to map the $\mathcal{Y}_4^{-3}$ real spherical harmonic to the g-wave symmetry profile of the altermagnetic order parameter in CrSb.

Contactless resistivity measurements

Contactless resistivity measurements were conducted using the proximity detector oscillator[53] technique in pulsed magnetic fields. A selected CrSb sample was mounted on a hand-wound planar coil of 15 turns, acting as the inductive component of the oscillator. The coil diameter was customized to match the sample width for optimal filling factor. A counter-wound outer coil enclosing the same area as the inner coil was added to compensate magnetic flux induced during the field pulse, minimizing background pickup.

As the applied magnetic field is swept, changes in the resistivity ρ and susceptibility χ_s of the sample lead to changes in the inductance of the oscillator and produce a shift in the resonant frequency of the oscillator, which can be described by

$$\frac{\Delta f}{f} \approx -\eta\frac{\delta}{d}\left(\mu_\mathrm{r}\frac{\Delta\rho}{\rho} + \Delta\chi_\mathrm{s}\right), \tag{7}$$

where η is the filling factor, d is the sample thickness, and $\mu_\mathrm{r} = 1 + \chi_\mathrm{s}$ is the relative magnetic permeability[53]. For a metallic material such as CrSb, eddy currents restrict the penetration of the radiofrequency field to a characteristic skin depth $\delta = \sqrt{2\rho/(\mu_\mathrm{r}\mu_0\omega)}$, where ω is the excitation frequency, such that the frequency response is dominated by changes in the resistivity ρ.

Proximity detector oscillator measurements reported in this study were performed in a 65-T pulsed magnet at the Dresden High Magnetic Field Laboratory in Dresden, Germany, following the methodology in ref. 54. A customized ^{3}He cryostat was fitted to the magnet, providing a base temperature of approximately 600 mK throughout the pulses. A raw resonant frequency of 25 MHz was achieved, which was fed into a heterodyne mixing circuit to down-convert the signal to about 10.5 MHz, which was subsequently acquired using a high-definition oscilloscope.

Quantum oscillatory components were analysed over a magnetic field range of 38–63 T using a LOESS background subtraction with an 8-T window and a second-order polynomial background subtraction. A quantum oscillation of frequency 0.8 kT was clearly resolved (Extended Data Fig. 7).

We note that, for sufficiently high magnetic fields, altermagnets have been predicted to exhibit certain distinguishing quantum oscillatory features, such as a distinct frequency splitting at a field-induced Lifshitz transition separating the up and down sheets[55]. However, we measured up to a maximal field strength of 64 T (Extended Data Fig. 7) and observed no such signatures. This is probably due to the very high ordering temperature (and hence energy scale) of altermagnetism in CrSb, which remains robust up to these large field strengths.

Data availability

The datasets supporting the findings of this study are available from the University of Cambridge Apollo Repository[56].

48. Eaton, A. G. et al. Quasi-2D Fermi surface in the anomalous superconductor UTe_2. *Nat. Commun.* **15**, 223 (2024).
49. Cleveland, W. S. & Devlin, S. J. Locally weighted regression: an approach to regression analysis by local fitting. *J. Am. Stat. Assoc.* **83**, 596–610 (1988).
50. Blaha, P. et al. WIEN2k: an APW+lo program for calculating the properties of solids. *J. Chem. Phys.* **152**, 074101 (2020).
51. Rourke, P. M. C. & Julian, S. R. Numerical extraction of de Haas–van Alphen frequencies from calculated band energies. *Comput. Phys. Commun.* **183**, 324–332 (2012).
52. Weinberger, T. Py_FS. *GitHub*. https://github.com/TheoWeinberger/py_FS (2023).
53. Altarawneh, M. M., Mielke, C. H. & Brooks, J. S. Proximity detector circuits: an alternative to tunnel diode oscillators for contactless measurements in pulsed magnetic field environments. *Rev. Sci. Instrum.* **80**, 066104 (2009).

54. Wu, Z. et al. Enhanced triplet superconductivity in next-generation ultraclean UTe_2. *Proc. Natl Acad. Sci. USA* **121**, e2403067121 (2024).
55. Li, Z.-X., Zhou, H., Wan, X. & Chen, W. Diagnosing altermagnetic phases through quantum oscillations. *Phys. Rev. B* **111**, 125119 (2025).
56. Long, M. et al. Research data supporting: 3D bulk-resolved *g*-wave altermagnetic order parameter in CrSb. University of Cambridge Apollo Repository https://doi.org/10.17863/CAM.131869 (2026).

Acknowledgements We thank A. J. Hickey, A. Agarwal, T. L. Lefebvre, J. Knolle, D. Candido, G. G. Lonzarich and N. J. M. Popiel for their discussions. We thank T. Haidamak, M. Vališka, H. Li, P. Einarsson Nielsen, H. Chen, R. Mann, T. J. Brumm and especially D. Sviták and S. Hayden for technical advice and assistance. We appreciate creative input from H. Weinberger.

Author contributions M.L., M.F.H. and R.T. grew single-crystal CrSb specimens. M.L. characterized the samples. M.L., T.I.W., Z.W., M.S., D.G., Y.S. and A.G.E. performed quantum oscillation experiments. M.L., T.I.W., Z.W., F.M.G. and A.G.E. analysed and interpreted the data. T.I.W. performed DFT calculations. A.G.E. conceived the project. F.M.G. and A.G.E. supervised the project. T.I.W., F.M.G. and A.G.E. wrote the paper, with input from all co-authors.

Funding This project was supported by the EPSRC of the United Kingdom (grant nos. EP/Z533695/1 and EP/R513180/1). A portion of this work was performed at the National High Magnetic Field Laboratory, which is supported by the National Science Foundation Cooperative Agreement (nos. DMR-1644779 and DMR-2128556) and the State of Florida. We acknowledge support of the Dresden High Magnetic Field Laboratory at Helmholtz-Zentrum Dresden-Rossendorf, a member of the European Magnetic Field Laboratory (EMFL), supported by EPSRC UK via its membership to EMFL (grant EP/N01085X/1). T.I.W. and A.G.E. acknowledge support from ICAM through the US National Science Foundation (grant no. 2201516) under the Accelnet program of the Office of International Science and Engineering and from QuantEmX grants from ICAM and the Gordon and Betty Moore Foundation (grant no. GBMF9616). T.I.W. acknowledges support from Murray Edwards College (University of Cambridge) and the Cambridge Philosophical Society through a Henslow Fellowship. A.G.E. acknowledges support from Sidney Sussex College (University of Cambridge).

Competing interests The authors declare no competing interests.

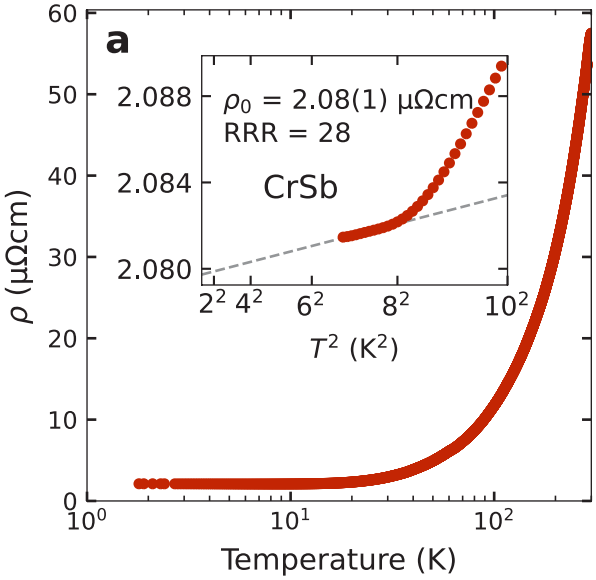
Additional information

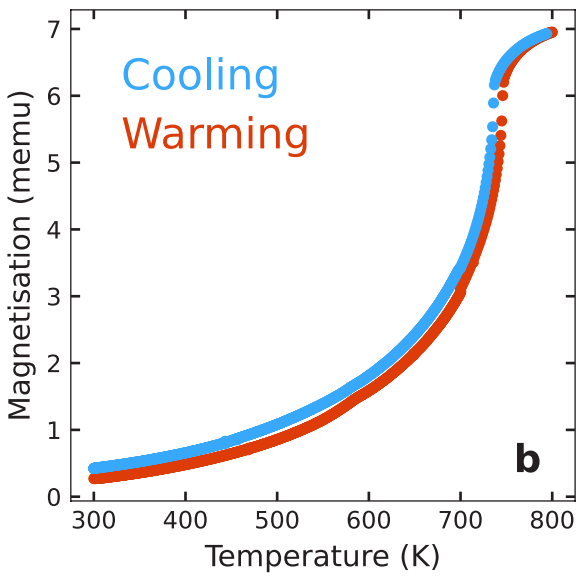
Supplementary information The online version contains supplementary material available at https://doi.org/10.1038/s41586-026-10902-z.

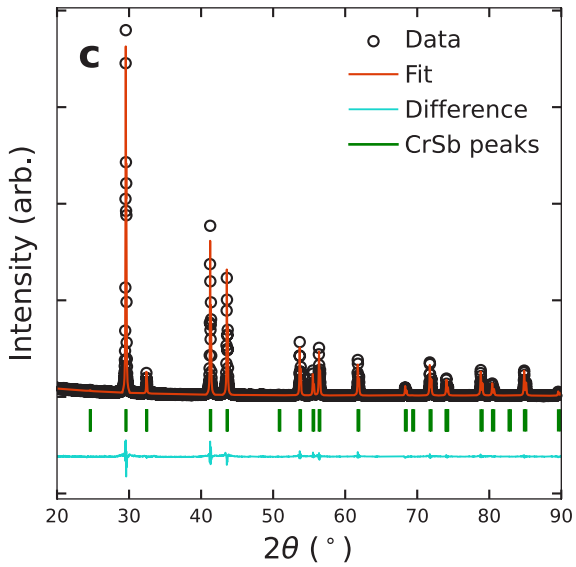
Correspondence and requests for materials should be addressed to Theodore I. Weinberger or Alexander G. Eaton.

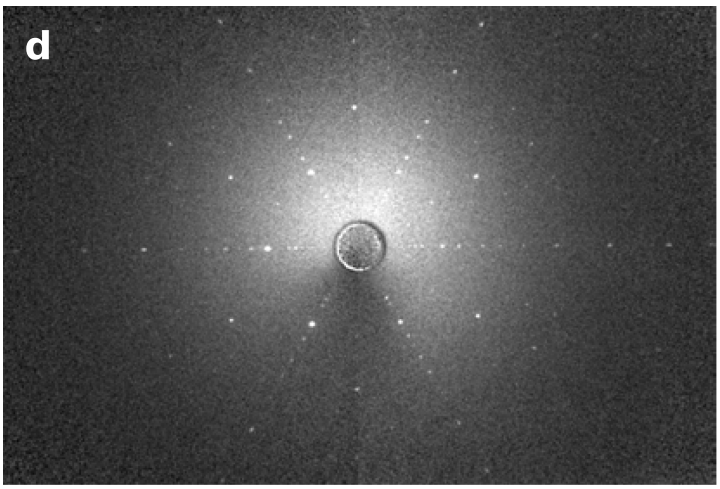
Peer review information *Nature* thanks Minghu Fang and the other, anonymous, reviewer(s) for their contribution to the peer review of this work. Peer reviewer reports are available.

Reprints and permissions information is available at http://www.nature.com/reprints.

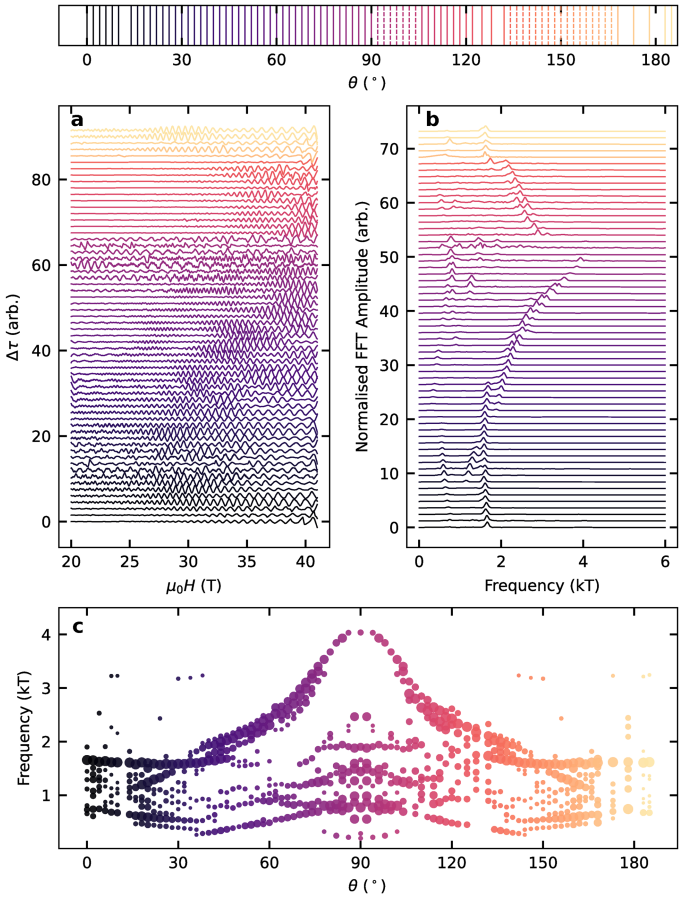




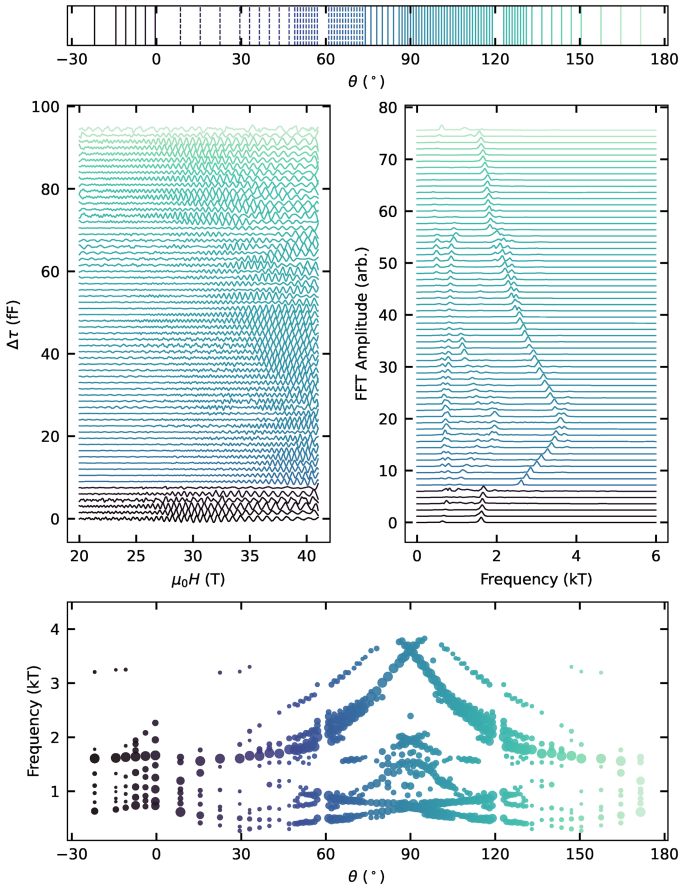




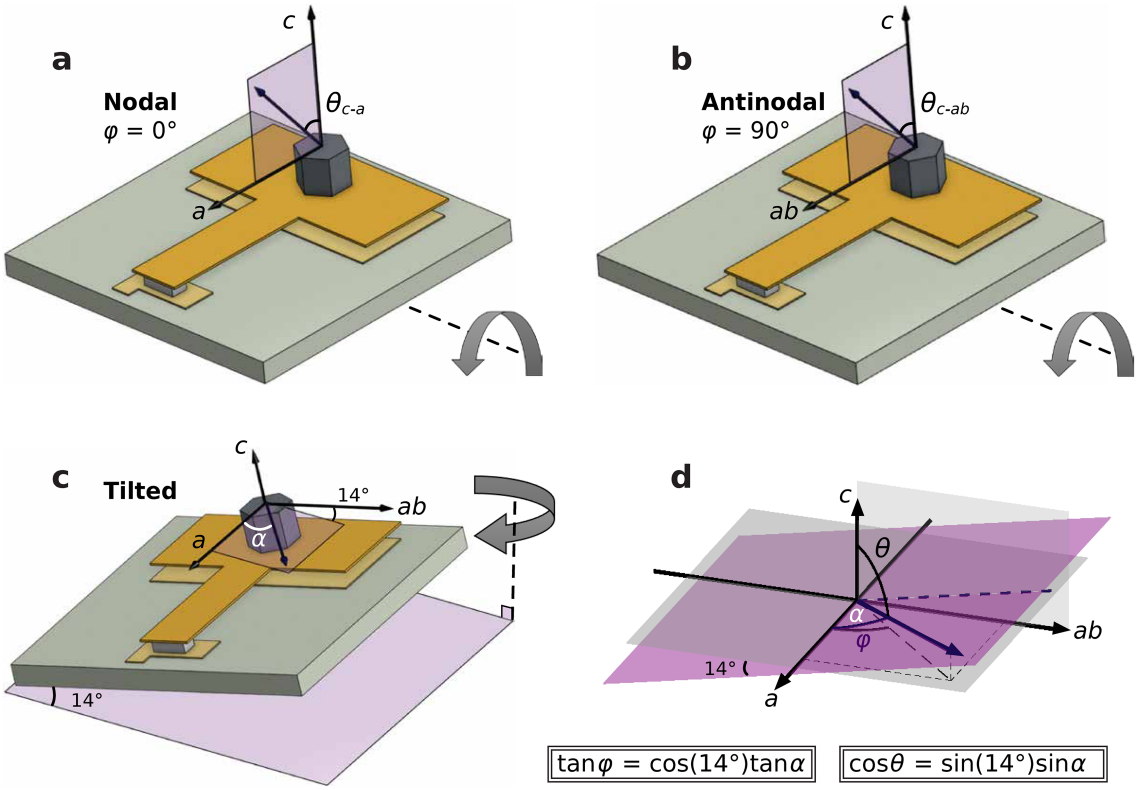
Extended Data Fig. 1 | Sample characterisation studies. a, Electrical resistivity ρ of CrSb measured by the four-terminal technique. The inset shows low temperature data fitted quadratically in temperature, to extract the residual resistivity of 2.08(1) μΩcm. This yields a residual resistivity ratio, upon dividing the 300 K resistivity by the fitted extrapolation to absolute zero, of RRR = 28. **b**, Magnetisation versus temperature up to 800 K, measured in a Quantum Design Magnetic Properties Measurement System with the furnace option mode under an applied field of 7 T. Red points were recorded on warming, with blue taken subsequently upon cooling. An anomaly at ≈ 740 K is resolved, indicating the onset of compensated collinear magnetic order. This is slightly higher than previously reported[41], likely due to improved crystal quality. **c**, Powder x-ray diffraction data plotted versus 2θ. The recorded data agree very well with the known structure[40] of CrSb. **d**, Lauegram of a single crystal specimen utilised in our quantum oscillation study. Sharp spots in a hexagonal pattern are clearly resolved, confirming single-crystallinity.



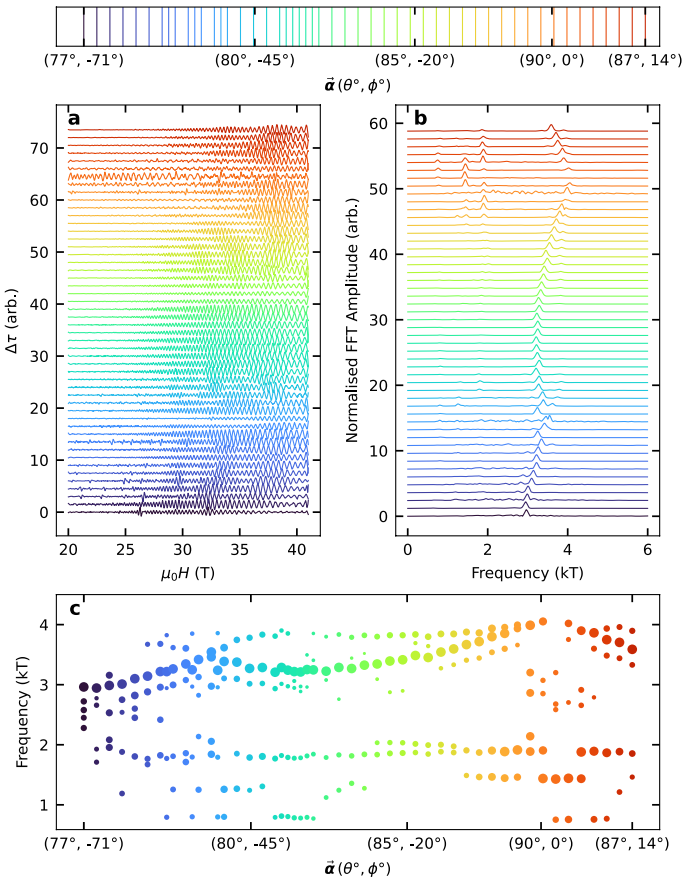
Extended Data Fig. 2 | Quantum oscillation measurements in the nodal *c*–*a* rotation plane. a, Normalised oscillatory component of magnetic torque Δτ, **b**, the corresponding fast Fourier transform spectra, and **c**, the frequency versus angle profile. A magnetic field range of 20-41 T was used, along with a LOESS window of 1.2 T and a second-order polynomial (see Methods). Dashed lines in the angular scale bar denote where symmetry-equivalent traces have been reflected through $\theta = 90°$, for display purposes in panel **c**. No spin-splitting is resolved in this nodal plane.



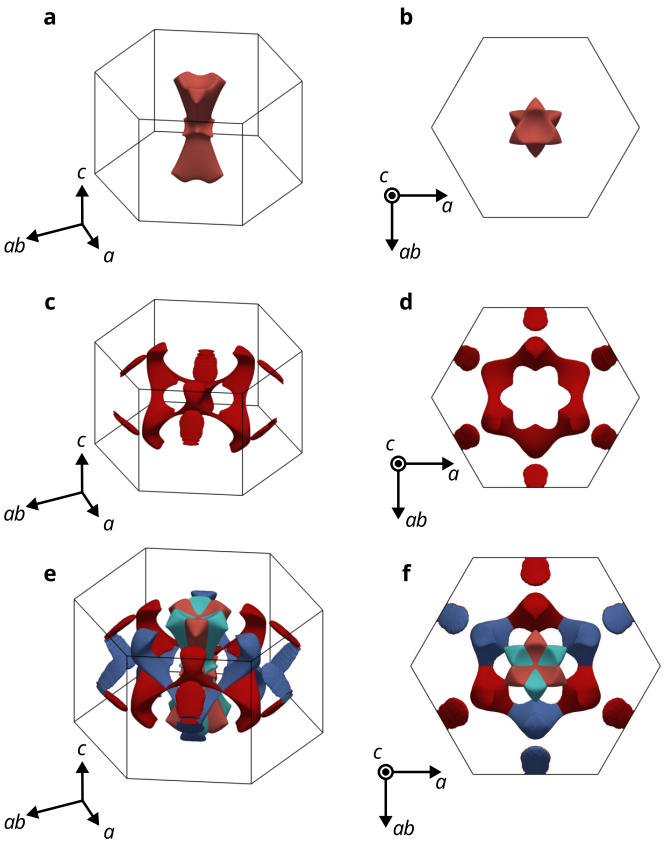
Extended Data Fig. 3 | Quantum oscillation measurements in the antinodal *c*–*ab* rotation plane. a, Normalised oscillatory component of magnetic torque $\Delta\tau$, **b**, the corresponding fast Fourier transform spectra, and **c**, the frequency versus angle profile. A magnetic field range of 20-41 T was used, along with a LOESS window of 1.2 T and a second-order polynomial (see Methods). Dashed lines in the angular scale bar denote where symmetry-equivalent traces have been reflected through $\theta = 90°$, for display purposes in panel **c**. Significant spin-splitting is resolved close to $\theta = 90°$, as shown clearly in Fig. 2.



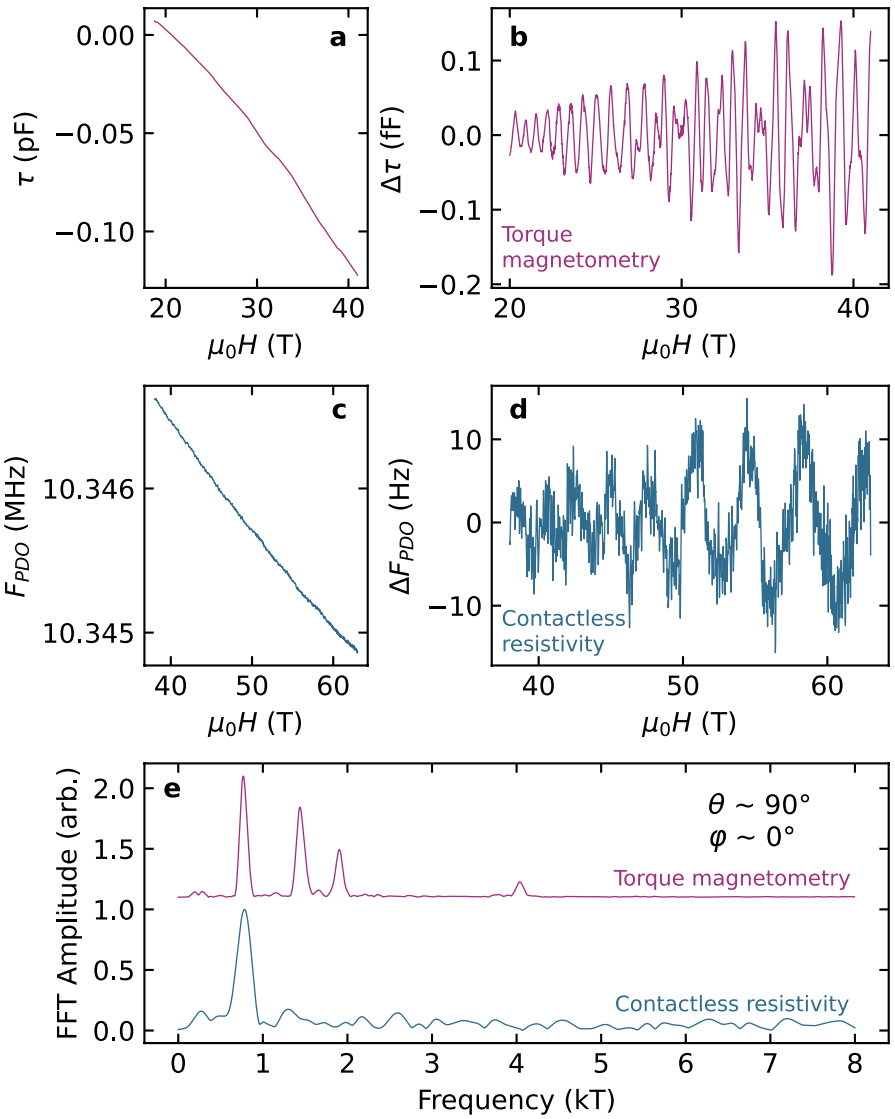
Extended Data Fig. 4 | Schematic diagrams of the rotational planes measured in this study. a, The relative crystal orientation with respect to the rotation axis for the nodal *c*–*a* rotation plane and **b**, the same for the antinodal *c*–*ab* plane. The dark grey hexagonal prism depicts the sample, which is mounted on a metallic cantilever narrowly suspended above a copper baseplate, therefore enabling capacitive torque magnetometry measurements. **c**, The tilted rotation plane for which data are presented in Fig. 3. The relative orientations of θ and φ with respect to the angle α are defined in **d**.



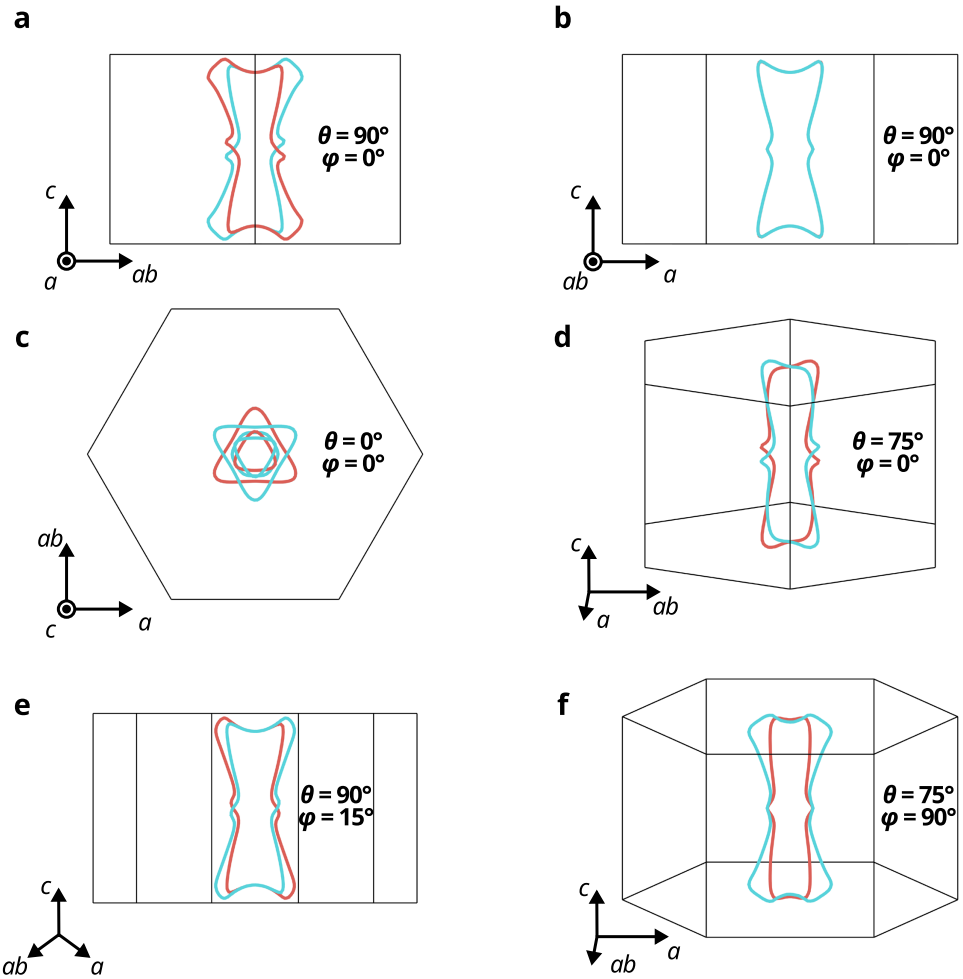
Extended Data Fig. 5 | Quantum oscillation measurements in a low-symmetry tilted rotation plane. a, Normalised oscillatory component of magnetic torque $\Delta\tau$, **b**, the corresponding fast Fourier transform spectra, and **c**, the frequency versus angle profile. A magnetic field range of 20-41 T was used, along with a LOESS window of 0.6 T and a second-order polynomial (see Methods). The rotation plane is defined in Extended Data Fig. 4. The high frequency branch undergoes significant spin-splitting away from nodal planes, as shown clearly in Fig. 3.



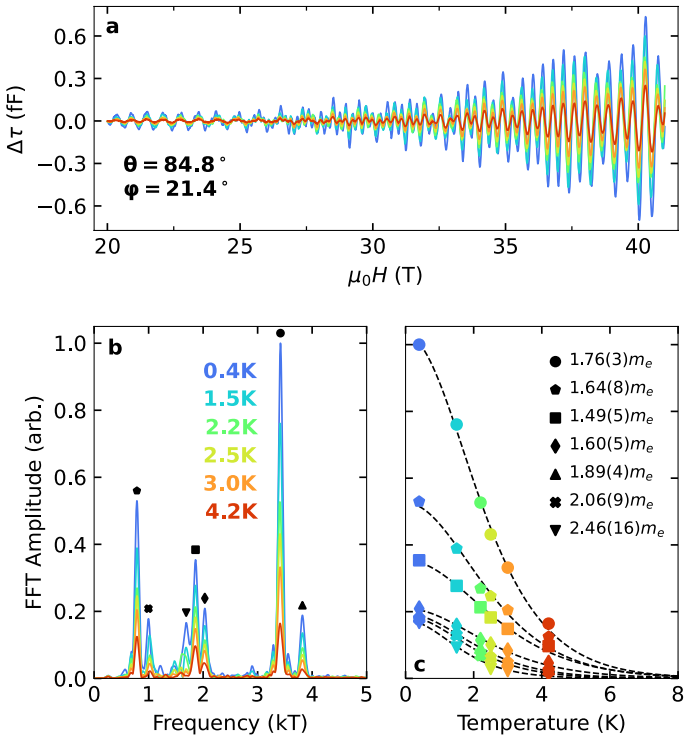
Extended Data Fig. 6 | Fermi surface renderings. a,**b**, The central (dogbone) Fermi sheet due to two hole-type bands that cross the Fermi level, and **c**,**d**, the secondary (web) sheet that results from two electron-type sheets crossing the Fermi level. For clarity, we plot only the up-sheets here. **e**,**f**, Spin-up (red) and spin-down (blue) sheets of the entire Fermi surface of CrSb.



Extended Data Fig. 7 | Pulsed magnetic field QO measurements. a, Capacitive torque magnetometry measured in steady fields and **b**, the background-subtracted oscillatory profile. **c**, Contactless resistivity measured by the PDO technique (see Methods) in pulsed fields and **d**, the background-subtracted oscillatory profile. **e**, FFT traces for both measurements, performed with the same magnetic field orientation. The signal-to-noise ratio of the contactless resistivity is insufficient to resolve the high frequency components, however the peak at 0.8 kT is well resolved. This frequency branch appears robust, with no sign of a Lifshitz transition, at least up to 64 T. Furthermore, the background contactless resistivity is quite smooth, showing no sign of e.g. a sudden reorientation of the magnetic moments.



Extended Data Fig. 8 | Comparison of orbital areas for different magnetic field orientations. a, Orienting magnetic field along the *a*-axis lies within a nodal plane, therefore the orbit for up-spins (red) can be mirrored through this plane onto a down-spin orbit. The result is that although the two orbits follow different paths in space, they are degenerate in area. Furthermore, applying fields along the **b**, *ab*-direction or **c**, *c*-direction induces quasiparticle orbits that are parallel to these nodal planes. If the up/down orbits lie in the nodal planes, they are truly degenerate in shape. If they lie above the planes, they can be mirrored to a matching orbit of the opposite spin below the plane. Magnetic fields applied within the **d**, *c*–*a* and **e**, *a*–*ab* planes lie along nodal directions. This produces orbits that follow different paths depending on the spin direction but are degenerate in area. **f**, Importantly, when the field is applied away from a nodal direction, but is not perpendicular to a nodal plane, we cannot use the 'reflective' symmetry that spin orbits hold about nodal planes to map up-spin orbits to down-spin orbits of equal area. Instead, quasiparticles orbiting around up- and down-sheets follow different paths of different areas. This results in QOs of different frequencies, characteristic of altermagnetic band splitting.



Extended Data Fig. 9 | Effective mass study. Fits to the Lifshitz-Kosevich temperature damping of quantum oscillatory amplitude. In Fig. 4 we high-pass filtered $\Delta\tau$ to focus on the Fourier components >3 kT that correspond to the dogbone pocket. Here we present the non-filtered background-subtracted torque signal, which includes significant spectral weight at lower frequencies due to the web sheet. We identify seven distinct peaks in the FFT spectrum (marked with symbols), which we fitted to the LK formula[14,46]. All peaks exhibit similar cyclotron effective masses, in the range $1.5 \leq m^*/m_e \leq 2.5$. This similitude of masses across the entire frequency range rules out the possibility of the high frequency components being either harmonics of lower components, or due to magnetic breakdown effects, as we detail in the Supplementary Information.

Extended Data Table 1 | DFT atomic positions

Atom	X	Y	Z
Cr_1	0.00	0.00	0.00
Cr_2	0.00	0.00	0.50
Sb_1	0.67	0.33	0.25
Sb_2	0.33	0.67	0.75

For the purposes of performing DFT calculations, we take two equivalent Cr positions, and likewise two equivalent Sb site locations, as specified.